HHS Public Access

Author manuscript

J Am Chem Soc. Author manuscript; available in PMC 2017 August 23.

Published in final edited form as:

J Am Chem Soc. 2016 February 24; 138(7): 2235–2243. doi:10.1021/jacs.5b12181.

Maximizing Electron Exchange in a [Fe_3] Cluster

Raúl Hernández Sánchez, **Amymarie K. Bartholomew**, **Tamara M. Powers**[†], **Gabriel Ménard**[‡], and **Theodore A. Betley**[*]

Department of Chemistry and Chemical Biology, Harvard University, 12 Oxford Street, Cambridge, Massachusetts 02138, United States

Abstract

The one-electron reduction of (^{tbs}L)Fe_3(thf)[1] furnishes [M][(^{tbs}L)Fe_3] ([M]$^+$ = [(18-C-6)K(thf)$_2$]$^+$ (1, 76%) or [(crypt-222)K]$^+$ (2, 54%)). Upon reduction, the ligand $^{tbs}L^{6-}$ rearranges around the triiron core to adopt an almost ideal C_3-symmetry. Accompanying the (^{tbs}L) ligand rearrangement, the THF bound to the neutral starting material is expelled, and the Fe–Fe distances within the trinuclear cluster contract by ~0.13 Å in 1. Variable-temperature magnetic susceptibility data indicates a well-isolated $S = {}^{11}/_{2}$ spin ground state that persists to room temperature. Slow magnetic relaxation is observed at low temperature as evidenced by the out-of-phase χ_{M}'' component of the alternating current (ac) magnetic susceptibility data and by the appearance of hyperfine splitting in the zero-field ^{57}Fe Mössbauer spectra at 4.2 K. Analysis of the ac magnetic susceptibility yields an effective spin reversal barrier (U_{eff}) of 22.6(2) cm^{-1}, nearly matching the theoretical barrier of 38.7 cm^{-1} calculated from the axial zero-field splitting parameter (D = −1.29 cm^{-1}) extracted from the reduced magnetization data. A polycrystalline sample of 1 displays three sextets in the Mössbauer spectrum at 4.2 K (H_{ext} = 0) which converge to a single six-line pattern in a frozen 2-MeTHF glass sample, indicating a unique iron environment and thus strong electron delocalization. The spin ground state and ligand rearrangement are discussed within the framework of a fully delocalized cluster exhibiting strong double and direct exchange interactions.

Graphical abstract

[*]**Corresponding Author:** betley@chemistry.harvard.edu.

[†]**Present Addresses:**

Department of Chemistry, Texas A&M University, College Station, Texas 77842, United States.

[‡]**Present Addresses:**

Department of Chemistry and Biochemistry, University of California Santa Barbara, Santa Barbara, California 93106, United States.

Supporting Information

The Supporting Information is available free of charge on the ACS Publications website at DOI: 10.1021/jacs.5b12181.

X-ray crystal structure images, Magnetic data, Mössbauer, Near-IR, FTIR and ^{1}H NMR spectra. (PDF)

Crystallographic data. (CIF)

Notes

The authors declare no competing financial interest.

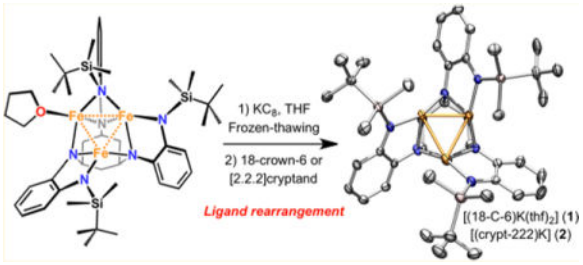

1. INTRODUCTION

High spin clusters feature prominently in nature, acting as the catalytic sites for small molecule activation (e.g., nitrogen fixation or water oxidation)[2] and as the biological circuitry for facilitating electron transfer.[3] The protein cofactors in nitrogenase and photosystem II must accumulate several reducing or oxidizing equivalents, respectively, before the activation of substrate can occur, achieving formally mixed-valent states within the cluster.[4] Mixed-valent iron–sulfur clusters[3] couple spin components via double exchange,[5] resulting in highest multiplicity ground state population and, more importantly, redox potential tuning.[6] As a design element of these cofactors, the ability to achieve large spin ground states enables electron transfer and redox load distribution over multiple sites, while also potentially enhancing cluster lability, allowing for facile geometric rearrangement during catalysis.

For both catalytic and electron-transfer proteins, double exchange coupling stabilizes the mixed-valent clusters.[6a,d] Unlike superexchange, which couples isovalent sites, double exchange couples two or more paramagnetic centers of differing valency linked by a bridging atom, ion, or molecule, or potentially interacting directly through M–M orbital overlap (direct exchange). The coupling consists of electron transfer mediated by either the bridging ligand or direct exchange pathways and favors ferromagnetic alignment between the two paramagnets.[7] In fact, a recent report describes a mixed-valent divanadium compound where the itinerant electron overrides the intrinsic antiferromagnetic coupling in the system.[8] Thus, in general, strongly delocalized mixed-valent aggregates typically exhibit thermally persistent, maximum spin ground states.[9]

We were thus interested in probing whether a molecule would geometrically rearrange undergoing redox to maximize the electron exchange interaction. An example of this phenomenon was shown by Lippard and co-workers, in which a dinuclear ferrous carboxylate-bound dimer rearranges upon one electron oxidation. The resulting mixed-valent lantern complex, where all four carboxylate ligands bridge the diiron unit, displays a contraction of the Fe–Fe distance from 4.219(1) Å in the diferrous starting material to 2.698(1) Å in the mixed-valent product.[10] It is worth noting that the diferrous starting material can also adopt the lantern orientation depending on the ancillary ligand used, and it is unclear whether the diferrous materials exhibit both structure types in solution. Thus, the structural equilibrium may be shifted upon oxidation to favor maximal delocalization of the oxidation load and depopulation of M–M antibonding orbitals, akin to M–M bonding observed in $[Mo_2]^{5+}$, $[Ru_2]^{5+}$, $[Os_2]^{5+}$, $[Rh_2]^{5+}$, and $[Pd_2]^{5+}$ examples.[11]

In our investigations on M–M bonding within clusters, we have published methods to synthesize tri-[1,12] and hexanuclear[13] clusters that allow systematic electronic structure tuning either by addition of exogenous ligands,[14] outer-sphere redox chemistry,[15] or by reaction with small molecules[16] affording mixed-valent products while retaining the initial cluster morphology. These types of clusters represent ideal species to investigate the effects of superexchange, direct exchange, and double exchange in the same cluster morphology as several redox states are readily accessible. Herein we report on the resulting properties of an all-ferrous trinuclear cluster (^{tbs}L)-Fe_3(thf) that undergoes cluster geometric reconfiguration upon reduction to maximize the electronic exchange coupling interaction within the cluster.

2. EXPERIMENTAL SECTION

2.1. General Considerations

All manipulations were performed under an atmosphere of dry, oxygen-free N_2 by means of standard Schlenk or glovebox techniques (MBraun glovebox equipped with a −35 °C freezer). Hexane, benzene, and tetrahydrofuran (THF) were dried and deoxygenated on a Glass Contour System (SG Water USA, Nashua, NH) and stored over 4 Å molecular sieves (Strem) prior to use. THF-d_8 was purchased from Cambridge Isotope Laboratories, degassed and stored over 4 Å molecular sieves prior to use. 18-crown-6 (18-C-6) and [2.2.2]cryptand (crypt-222) were purchased from Sigma-Aldrich and dried by dissolving in diethyl ether and storing over sieves for several days, followed by removal of the sieves and solvent. ^{tbs}LH6,[1] (^{tbs}L)Fe_3(thf) (see Supporting Information), and potassium graphite (KC_8)[17] were prepared according to literature procedures. All other reagents were purchased from commercial vendors and used without further purification.

2.1.1. [(18-C-6)K(thf)$_2$][(^{tbs}L)Fe_3] (1)—A scintillation vial equipped with a magnetic stir bar was charged with KC_8 (15.2 mg, 0.11 mmol) and THF (5 mL). The mixture was frozen in the liquid N_2–cooled cold well. To the frozen mixture was added a solution of (^{tbs}L)Fe_3(thf) (100 mg, 0.10 mmol) dissolved in THF (5 mL). The frozen solution was thawed and stirred rapidly at r.t. for 2 h after which 18-crown-6 (29.7 mg 0.11 mmol) was added. The solution was stirred for another 15 min prior to solvent removal in vacuo. The black residue was washed with hexane (ca. 5 mL) and filtered on a pad of Celite. The black solid on top of the pad of Celite was further washed with benzene (ca. 5 mL) until the filtrate solution was colorless. The remaining black solid was recovered by dissolving with THF (ca. 10 mL) and pushing this solution through the Celite. THF was added until the filtrate solution was colorless. Diethyl ether (ca. 5 mL) was added to the solution and the vial was cooled to −35 °C yielding pure black crystals of product after 24 h (105 mg, 78 μmol, 76%). The pure crystals obtained were suitable for X-ray diffraction studies. ^{1}H NMR (600 MHz, THF-d_8): δ 86.7 (b), 46.5 (b), 18.9 (b), 3.62 (THF-h$_8$), 2.96 (18-crown-6), 1.79 (THF-h$_8$). Anal. Calc. for $C_{62}H_{106}Fe_3KN_6O_8Si_3$: C, 54.98; H, 7.89; N, 6.20. Found: C, 54.85; H, 7.81; N, 6.08.

2.1.2. [(crypt-222)K][(^{tbs}L)Fe_3] (2)—A scintillation vial equipped with a magnetic stir bar was charged with KC_8 (27.6 mg, 0.20 mmol) and THF (4 mL). The mixture was frozen in the liquid N_2-cooled cold well. To the frozen solution was added a solution of

(^{tbs}L)Fe_3(thf) (200 mg, 0.20 mmol) dissolved in THF (8 mL). The frozen solution was thawed and stirred rapidly at r.t. for 1.5 h and then filtered through a pad of Celite, after which [2.2.2]cryptand (75.3 mg, 0.20 mmol) was added. The solution was stirred for 1 h at r.t. at which point a fine black precipitate began to form. The solution was then cooled to −35 °C. After cooling, the precipitate was collected on a fritted funnel and washed thoroughly with hexanes (30 mL) and diethyl ether (30 mL), until the filtrate solution was colorless. The solid was then dried in vacuo to yield the product as a fine black powder (146.8 mg, 0.11 mmol, 54%). Crystals suitable for X-ray diffraction studies were grown from a concentrated THF solution at −35 °C. ^{1}H NMR (500 MHz, THF-d_8): δ 84.0 (b), 46.6 (b), 18.5 (b), 4.19 ([2.2.2]cryptand), 3.32 ([2.2.2]cryptand), 2.35 ([2.2.2]cryptand), −139.4 (b). Bulk purity of 2 was determined by zero-field ^{57}Fe Mössbauer analysis of a bulk sample that registered identical to 1 at 90 K (Figure S7), multiple crystals were mounted to confirm the constitution via single crystal analysis, and 100 K magnetization analysis to check for ferromagnetic impurities.

2.2. X-ray Structure Determinations

Single crystals suitable for X-ray structure analysis were coated with deoxygenated Paratone N-oil and mounted in MiTeGen Kapton loops (polyimide). Data for 1 and 2 were collected at 100 K on an APEX II CCD or APEX II DUO singlecrystal diffractometer. None of the crystals showed significant decay during data collection. Raw data was integrated and corrected for Lorentz and polarization effects using Bruker APEX2 v.2009.1.[18] Absorption corrections were applied using SADABS.[19] Space group assignments were determined by examination of systematic absences, E-statistics, and successive refinement of the structures. The program PLATON[20] was employed to confirm the absence of higher symmetry. The positions of the heavy atoms were determined using direct methods using the program SHELXTL.[21] Successive cycles of least-squares refinement followed by difference Fourier syntheses revealed the positions of the remaining non-hydrogen atoms. Non-hydrogen atoms were refined with anisotropic displacement parameters, and hydrogen atoms were added in idealized positions. Crystallographic data for **1** and **2** is given in Table S1.

2.3. Zero-Field ^{57}Fe Mössbauer Spectroscopy

Data was collected from 4.2 to 210 K for a polycrystalline solid (ca. 80 mg) of 1 restrained in Paratone-N oil and as a frozen glass at 4.2 K (2-methyltetrahydrofuran). The data was measured with a constant acceleration spectrometer (SEE Co., Minneapolis, MN). Isomer shifts are given relative to α-Fe metal at 298 K. The 4.2 K data was fit using WMOSS4,[22] while the 210 K data was analyzed using an in-house package written by E. R. King in Igor Pro (Wavemetrics). γ refers to the full-width-at-half-maximum (fwhm).

2.4. Electrochemical Measurements

Cyclic voltammetry measurements were acquired on a CHI660d potentiostat. A three-electrode cell setup was used with a 3 mm diameter glassy carbon working electrode, Pt wire counter electrode, and $Ag/AgNO_3$ reference electrode. Saturated $AgNO_3$ solutions in MeCN for the reference electrode were prepared fresh before each experiment. All measurements

were done under a dinitrogen atmosphere and at room temperature. A 0.1 M solution of tetrabutylammonium hexafluorophosphate in THF was used as the supporting electrolyte.

2.5. Magnetic Data Measurements

Magnetic data for 2 was collected using a Quantum Design MPMS-XL Evercool SQUID Magnetometer. The general sample preparation procedure consisted of placing polycrystalline powder of 2 into a gelatin capsule size #4. This powder was immobilized by adding melted eicosane at 50–60 °C. The gelatin capsule was then inserted into a plastic straw. Samples were prepared under a dinitrogen atmosphere. Magnetization data at 100 K from 0 to 7 T was used as a ferromagnetic-free purity test (Figure S9). Direct current (dc) variable-temperature magnetic susceptibility measurements were collected in the temperature range 5–300 K under an applied field of 0.5 T. Low temperature magnetization data was acquired on heating from 1.8 to 10 K at increasing magnetic fields of 1, 2, 3, 4, 5, 6, and 7 T. Magnetic susceptibility data was corrected for diamagnetism of the sample, estimated using Pascal's constants, in addition to contributions from the sample holder and eicosane. The magnetic susceptibility data was collected multiple times until at least three different batches reproduced the data; these three passed the ferromagnetic-free purity test. The $\chi_M T$ and reduced magnetization data were modeled in *PHI*[23] according to the spin Hamiltonian described in the main text. Alternating current (ac) magnetic susceptibility data was collected at zero-applied dc field and with an oscillating 4 Oe ac field.

2.6. Other Physical Measurements

NMR spectra were recorded on an Agilent DD2 600 MHz or Varian 500 MHz spectrometer and the spectra were referenced to residual solvent (THF-d_8: ^{1}H = 1.72 and 3.58 ppm), with chemical shifts listed in ppm. Elemental analyses were performed by Complete Analysis Laboratories, Inc., Parsippany, New Jersey. UV–vis–NIR spectra were collected in 1 mm path length cuvettes on a Varian 5000 spectrophotometer. All solutions were prepared under N_2 atmosphere in a glovebox and the cuvettes sealed with a J-Young Teflon cap. Absorbance values were kept under 1.

3. RESULTS

3.1. Synthesis and Characterization

The all-ferrous triiron cluster (^{tbs}L)Fe$_3$(thf) was synthesized using a slight modification (see the Supporting Information) of the reported synthesis by metalation of the hexadentate amine ligand ^{tbs}LH$_6$ (1,3,5-(^{t}BuMe$_2$SiNH-*o*-C$_6$H$_4$NH)$_3$C$_6$H$_9$) with 1.5 equiv of Fe$_2$(N(SiMe$_3$)$_2$)$_4$ in THF.[1] Substitution of the more thermally robust Fe$_2$(N(SiMe$_3$)$_2$)$_4$ for Fe$_2$(Mes)$_4$ allows for higher yields of purer material to be obtained (Mes = 2,4,6-Me$_3$C$_6$H$_2$). As reported earlier,[1] the solid state molecular structure of (^{tbs}L)Fe$_3$(thf) features an asymmetric core where each of the three iron sites is geometrically distinct. The three secondary anilido ligand units directly attached to the ligand cyclohexane base bridge adjacent metal centers, creating a chairlike conformation for the [Fe$_3$N$_3$] base of the cluster (illustrated in Scheme 1). The large *tert*-butyldimethylsilyl (tbs) groups sterically restrict two of the three peripheral anilido groups to bind terminally to two of the iron sites, allowing only one peripheral anilido group to bridge between two iron sites. One of the two four-

coordinate iron sites features an all-N coordination sphere derived exclusively from the ($^{tbs}L^{6-}$) platform; whereas the adjacent four coordinate site binds one THF molecule to complete its coordination sphere. The remaining iron site within the cluster remains three coordinate in a nominally T-shaped geometry bound to two basal anilido units and one terminal anilido group. Whereas the sterically less encumbered ($^{H}L^{6-}$) and ($^{Ph}L^{6-}$) ligand variants optimally direct a subset of the iron valence orbitals within the cluster to maximize intracluster orbital overlap by having their d_z^2 orbitals contained within the triiron plane,[12,14] the direct orbital exchange pathways between the iron sites in (^{tbs}L)Fe_3(thf) are less obvious. Nevertheless, the close Fe–Fe contacts (d_{avg}: 2.577(35) Å) still permit sufficiently strong interactions for (^{tbs}L)Fe_3(thf) to possess a maximally high spin ($S = 6$) ground state.[1]

Reduction of (^{tbs}L)Fe_3(thf) was accomplished by adding a THF solution of the all-ferrous cluster to a frozen suspension of KC_8 in THF. The reaction mixture was stirred vigorously while thawing to room temperature over the course of 2 h after which 18-crown-6 or [2.2.2]cryptand was added. The reduced clusters [(18-C-6)K(thf)$_2$][(^{tbs}L)Fe_3] (**1**) and [(crypt-222)K][(^{tbs}L)-Fe_3 (**2**) were isolated in 76% and 54% yield following workup (Scheme 1), respectively, and their composition determined via single-crystal X-ray crystallography. The ^{1}H NMR spectrum of **1** obtained in THF-d_8 displays only four broad resonances (δ) at 2.96 (assigned to the 18-C-6), 18.9, 46.5, and 86.7 ppm (Figure S3), whereas for **2** seven broad resonances are observed at −139.4, [2.35, 3.32, 4.19] (assigned to [2.2.2]cryptand), 18.5, 46.6, and 84.0 ppm (Figure S4). While largely uninformative, the ^{1}H spectrum of **1** should be contrasted with its all-ferrous precursor (^{tbs}L)Fe_3(thf), which is ^{1}H NMR silent.[1]

3.2. Molecular Crystal Structure

Large single crystals, up to 2 × 2 × 4 mm in size, suitable for single crystal X-ray diffraction studies were afforded by cooling concentrated solutions of **1** in a mixture of THF:Et_2O. The crystal structure of the anion of **1** is presented in Figure 1a. The THF solvent molecule from the all-ferrous precursor has been expelled, and the triiron cluster reconfigures its overall conformation to accommodate a helical disposition of the ligand ($^{tbs}L^{6-}$), leaving each of the (^{tbs}L) peripheral anilido groups terminally bound to a unique iron site. The triiron anion resides in an almost idealized C_3 symmetric geometry, though the presence of the 18-C-6 encapsulated K^+ prevents true crystallographic C_3 symmetry from being realized. The anion's C_3 axis is normal to and passes through the geometric mean of the triiron plane. Whereas in the all-ferrous parent cluster three distinct coordination sites were observed, each of the iron sites in **1** resides in a three-coordinate, distorted T-shaped geometry [∠N–Fe–N_{avg} (deg): 86.1(1), 100.9(6), 158(1)] akin to the three-coordinate site in (^{tbs}L)Fe_3(thf). Each of the [N_3Fe] planes is canted with respect to the triiron plane yielding dihedral angles ∠[N_3Fe]–Fe_3 (deg) of 52.26(13), 54.30(13), and 54.77(13) (52.31(13), 53.08(15), and 54.42(14) for **2**). The Fe–Fe distances are significantly affected upon chemical reduction of (^{tbs}L)Fe_3(thf). The Fe–Fe separation in **1** contracts by an average of nearly 0.13 Å relative to the Fe–Fe distances in the parent all-ferrous species. The core Fe–Fe metrics for (^{tbs}L)Fe_3(thf) (distances indicated in black) and **1** (distances indicated in red) are compared in Figure 1b. Statistically relevant metrical changes are also manifest within the Fe–$N_{Si,\ avg}$

and Fe–$N_{basal, avg}$ distances (2.029(51) and 2.048(24) to 1.942(2) and 2.027(12) Å in **1**, respectively) and ∠Fe–N–Fe_{avg} angle (77.5(10) to 74.2(4)° in **1**, see Table S2). In related mixed-valent hexairon clusters embedded within similar weak-field ligand environments, the contraction in the Fe–N_{avg} distance correlates linearly with a decrease in the spin ground state.[24]

3.3. Electrochemical and Near-Infrared Absorption Data

The electrochemical behavior of **1** was investigated in THF. Scanning anodically from the open circuit potential of **1** at −2.0 V two oxidation events are found at −1.71 and −1.18 V vs Fc/Fc^+ (Figure 1c bottom). The redox events observed under these conditions indicated by the green and blue traces are quasi-reversible. While the first one-electron oxidation affords the neutral all-ferrous species, the subsequent oxidation suggests the monocationic species $[(^{tbs}L)Fe_3]^+$ is accessible, though such a species has thus far eluded chemical isolation. Analysis of the first one-electron oxidation event displays a dependence of the peak-to-peak potential (ΔE_p) with the scan rate (Figure S5) and likely arises from the structural reorganization upon electron transfer.

Scanning cathodically, **1** can be electrochemically reduced, displaying a cathodic peak potential (E_{pc}) of −3.29 V vs Fc/Fc^+ Isolation of this highly reduced species has not been attempted. The comproportionation constant (K_c) measured electrochemically is an indicator of the extent of electron sharing or delocalization, and thus a strong indicator of the stability of the mixed-valence species.[25] Worth noting, the experimental conditions used in the voltammetric determination may change the overall magnitude of K_c considerably.[26] From the data in Figure 1c bottom we obtain $K_c < 9.9 \times 10^{26}$ for **1**.

The appearance of intervalence charge transfer (IVCT) bands in the near-infrared spectral region are highly indicative of mixed-valence compounds.[27] The first model to describe these metal-to-metal charge transfers was put forward by Hush.[28] The extent of delocalization in mixed-valence compounds was classified into three categories: Class I corresponds to redox-localized compounds, Class II signifying partial delocalization, and a Class III designation for fully delocalized systems.[29] A fully delocalized, Class III compound has zero thermal barriers to electron transfer. Thus, the two adiabatic ground state energy surfaces of the reactants and products share a single minimum.[30] Surprisingly, the near-IR (THF, 25 °C) and IR (KBr pellet) spectra for compound 1 do not feature any absorption bands attributable to an IVCT in the energy region between 800–3300 nm as shown in Figure 1c (NIR) top and Figure S13 (IR).

3.4. Magnetometry

To avoid complications with desolvation of the countercation in **1**, the analogous THF-free compound **2** was synthesized and used for the magnetometric studies. The electronic structure of **2** was investigated in more detail by collecting magnetic data under static (dc) and oscillating (ac) magnetic fields. Variable-temperature dc magnetic susceptibility was collected from 5 to 300 K at 0.5 T (Figure 2a). The susceptibility ($\chi_M T$) plateaus above 15 K at a value of 18.9 ± 0.1 cm^3 K/mol. Below 15 K a pronounced drop in $\chi_M T$ is observed to 16.1 cm^3 K/mol at 5 K, likely the result of zero-field splitting. The value of $\chi_M T$ over the

temperature range surveyed is consistent with an $S=^{11}/_{2}$ configuration, where the spin-only value anticipated is 17.875 cm^3 K/mol. We modeled the magnetic susceptibility data given in Figure 2a as a *single spin* manifold comprised of the three iron sites in 2.

The susceptibility data was then fit using the following spin Hamiltonian $\hat{H}=D\hat{S}_z^2+g_{\mathrm{iso}}\mu_B \mathrm{S}\cdot\mathrm{H}$ considering an $S=^{11}/_{2}$. The data was well reproduced with the fit parameters g = 2.05 and $|D|$ = 0.15 cm^{-1} as illustrated in Figure 2a with the red trace (raw data provided in blue circles). To gain more insight into the ground state of **2** and more accurate zero-field splitting parameters, variable-temperature, variable-field (VTVH) magnetization data was collected on heating from 1.8 to 10 K and at increasing fields of 1 to 7 T (Figure 2a inset). Magnetization saturation occurs at 8.98 μ_B at 1.8 K and 7 T. The lower than expected saturation (11 μ_B for an ideal $S=^{11}/_{2}$ with g =2) and the observation of nonsuperimposable isofield curves indicates the presence of zero-field splitting, which was quantified by fitting the data to the spin Hamiltonian. $\hat{H}=D\hat{S}_z^2+E(\hat{S}_x^2-\hat{S}_y^2)+g_{\mathrm{iso}}\mu_B \mathrm{S}\cdot\mathrm{H}$ The fit parameters considering an $S=^{11}/_{2}$ that best reproduce the data are g = 2.06, D = −1.29 cm^{-1}, $|E/D|$ = 0.33 (Figure 2a inset, continuous black traces). Moreover given the almost ideal C_3 symmetry of **2** a second scenario to fit the VTVH magnetization data was considered where $|E/D|$ = 0.[31] The fit parameters obtained are g = 2.06, D = −1.19 cm^{-1}, $|E/D|$ fixed to 0 (Figure S11b). Both the $\chi_M T$ and VTVH magnetization data was fit using the software *PHI*.[23]

3.5. Slow Magnetic Relaxation Phenomena

3.5.1. AC Magnetic Susceptibility—Slow magnetic relaxation behavior in $[(^{tbs}L)Fe_3]^-$ was evident from early investigations of **1** and **2** via zero-field ^{57}Fe Mössbauer spectra collected at 90 K (vide infra, Figure S6 and S7). To explore the magnetic relaxation dynamics of **2** further, variable-frequency, variable-temperature ac magnetic susceptibility data was collected under an oscillating field (1 to 1488 Hz) of 4 Oe from 2.2 to 3.6 K at zero-applied dc field (Figure 2.b1–b4).

The maximum observed in the out-of-phase (χ_M'', Figure 2.b1), in addition to the decrease in the in-phase component (χ_M', Figure 2.b3) between 2.2 and 3.6 K are the classic signatures of slow relaxation of the magnetization.[32] Similarly, the slow relaxation of the magnetization can also be seen by the maxima displayed in the χ_M'' vs T plot in Figure 2.b2. Additionally, magnetic data are customarily analyzed via Cole–Cole plots (χ_M'' vs χ_M', Figure 2.b4) where each semicircle observed indicates a distribution of a single relaxation pathway.[33] The χ_M'' vs χ_M' data was analyzed according to a generalized Debye model.[34] To effectively model the data in Figures 2.b1, b3, and b4, a single relaxation process with a distribution of time constants around τ was employed as described elsewhere.[35] Relaxation times were also extracted by employing the relationship $\omega\tau$ = 1 at the maxima of the χ_M'' vs T plot (Figure 2.b2).[36]

All four panels in Figure 2.b1–b4 were fit independently (continuous lines) and the extracted temperature-dependent relaxation times (τ) fit to an Arrhenius temperature law of the form: $= {}_0\exp(U_{eff}/k_BT)$. The mean value of the extracted spin reversal barrier (U_{eff}) is 22.6(2) cm^{-1} with a relaxation attempt frequency of $\tau_0 = 2.1(3) \times 10^{-8}$ s (Figure 2c). From this data a magnetic blocking temperature (T_B) of 1.45 K can be calculated as defined by Gatteschi et al. ($\tau = 100$ s).[32]

3.5.2. VT Zero-Field ^{57}Fe Mössbauer Spectroscopy—Slow relaxation of the magnetization was also observed via Mössbauer spectroscopy under zero-applied external magnetic field (Figure 3). The initial communication on the all-ferrous (^{tbs}L)Fe_3(thf) cluster reported a broad spectrum at 90 K that was fit to three distinct electric field gradients (signifying three distinct iron environments).[1] Nonetheless, when the temperature of acquisition is lowered to 4.2 K, a multiline spectrum for (^{tbs}L)Fe_3(thf) is obtained (Figure S8), as observed in other molecular species.[24,37] The spectral features are broad and unresolved, consistent with overlapping sextets, indicative of a slowly relaxing internal magnetic field (H_{int}). However, the magnetic relaxation rate exceeds that which is needed to display an out-of-phase χ''_M signature in the ac magnetic susceptibility under zero-applied dc field since no maximum is observed, even at the lowest temperatures achievable (1.8 K).

The ^{57}Fe Mössbauer spectrum obtained for the one-electron reduced cluster **1** is significantly different from its all-ferrous precursor. Unlike the spectrum of (^{tbs}L)Fe_3(thf) which displays three overlapping quadrupole doublets, the spectrum of **1** at 90 K displays an asymmetric doublet (Figure 3f and S6, for **2** see Figure S7). Moreover, the 4.2 K data displays a clear, well-resolved hyperfine-split spectrum (Figure 3a). The data collected on a polycrystalline sample at 4.2 K features more than a six-line pattern spectrum, suggesting this to be a composite of three distinct components. This is consistent with the structure for **1** obtained at 100 K wherein each of the iron sites is crystallographically distinct.

To examine whether the spectral features of polycrystalline **1** were manifest due to solid-state packing effects, the spectrum for **1** was reacquired at 4.2 K in a frozen glass using 2-methyltetrahydrofuran (Figure 3b). The spectral composite for the polycrystalline sample in Figure 3a simplifies to only one six-line pattern, suggesting a geometric equivalence of the iron coordination sites in solution. The spectrum of the polycrystal-line sample was fit in WMOSS4[22] to three iron environments according to the nuclear Hamiltonian $\hat{H} = \mathbf{I}\cdot\mathbf{Q}\cdot\mathbf{I} + g_n\beta_n\mathbf{H}\cdot\mathbf{I}$;[38] where Q is proportional to the electric field gradient and the internal field (H_{int}) is the only contribution to the total magnetic field (since $H_{ext} = 0$). H_{int} develops from the slow relaxation of the electronic ground state $|S, m_s\rangle$ as described above.[37f] The three sextets that reproduce the data in Figure 3a have the following parameters [δ, ΔE_Q (mm/s), H_{int} (T): 0.45, 1.34, 25.1 (33%, blue trace); 0.46, 1.40, 27.5 (33%, green trace); and 0.63, 1.40, 22.7 (34%, brown trace)]. Using the same fitting algorithm, the data in Figure 3b was reproduced by a single sextet with [δ, ΔE_Q (mm/s), H_{int} (T): 0.50, 1.22, 26.0]. Generally at high temperatures the internal field averages to zero and the ground and excited nuclear spin states are no longer Zeeman split; thus the data can be fit considering only the quadrupolar interaction.[37a] In this regard, the spectrum for **1** obtained at 210 K (Figure 3i) was fit (red trace) with parameters [δ and $|\Delta E_Q|$ (mm/s): 0.45, 1.94].

4. DISCUSSION

One-electron reduction of (^{tbs}L)Fe$_3$(thf) affords [M][(^{tbs}L)Fe$_3$] ([M]$^+$ = [(18-C-6)K(thf)2]$^+$ (**1**) or [(crypt-222)K]$^+$ (**2**)). Remarkably, the crystal structure of **1** (and **2**) displays the ^{tbs}L^{6-} ligand rearranged around the [Fe$_3$]-core with THF expulsion to produce an almost idealized C_3-symmetric geometry. Thus, the geometric rearrangement must energetically compensate for the loss of the two-electron donation from solvent binding. Indeed the cluster reorganization occurs with concomitant contraction in the mean Fe–Fe distance of 0.13 Å. We surmise the M–M intracore contact contraction maximizes the direct Fe–Fe valence orbital overlap, and therefore intracore M–M bonding, with respect to its asymmetric precursor. A similar geometric reconfiguration and shortening of M–M separation was observed upon oxidation of a diiron tetracarboxylate complex.[10] While the M–M contraction in lantern complexes is consistent with depopulation of M–M antibonding orbitals following oxidation, **1** and **2** exhibit similar geometric contractions upon reduction. Thus, M–M bonding is maximized when the metal sites are geometrically equivalent (maximizing double exchange) while residing in a high spin configuration where all M–M antibonding interactions are populated (vide infra).

Strong electron delocalization was ascertained by one of the largest known to date comproportionation constants found for **1** (K_c < 9.9 × 10^{26}), well beyond the threshold defined for a fully delocalized Class III species (K_c = 10^8 for the classic Creutz-Taube ion {[(H$_3$N)$_5$Ru]$_2$(pyr)}$^{5+}$).[25,30] Although an IVCT band in the near-IR was expected,[39] a flat, featureless absorption spectrum is obtained for **1** between 800 and 3300 nm. Similarly, other strongly delocalized compounds have shown intense bands toward the red in the visible region and none in the near-IR,[9c] or very weak bands in the near-IR not assignable to IVCTs.[9g] For fully delocalized species the energy of the IVCT band is spin dependent and is given by $E_{op}(S) = 2|B|(S + 1/2)$, where B represents the double exchange interaction energy.[6b] It is possible that such IVCT band in **1** exists outside the range of our current measurements, providing an upper limit for B of ~250 cm^{-1}.

VT magnetic susceptibility display a well-isolated $S = {}^{11}/_{2}$ up to 300 K. A complement to the ground state assignment comes from analyzing the $\chi'_{M}T$ data at low frequencies where it mimics the dc experiment but using significantly smaller magnetic fields.[40] The $\chi'_{M}T$ vs T plot shown in Figure S10 displays a smooth monotonic increase above 2.4 K to the ideal value of 17.875 cm^3 K/mol for an $S = {}^{11}/_{2}$ (g = 2). The abrupt decrease below 2.4 K correlates with slow magnetic relaxation effects.[41] The ground state was also investigated at low temperature via VTVH magnetization from where the axial (D) zero-field splitting parameter was extracted and used to calculate the expected spin reversal barrier U of 38.7 and 35.7 cm^{-1} by aplying $U = |D|(S^2 - 1/4)$, where $S = {}^{11}/_{2}$ and D = −1.29 or −1.19 cm^{-1}, respectively (Figure S11a,b). In practice the expected and effective U differ significantly due to tunneling of the magnetization.[42] The observed U_{eff} (22.6(2) cm^{-1}) represents about half of the theoretical spin reversal barrier U in 2 and likely corresponds to the energetic difference of the M_S = ±11/2 and ±7/2 (23.22 and 21.42 cm^{-1} for D = −1.29 or −1.19 cm^{-1}, respectively). In general the majority of SMMs reported to date have $U_{eff} \ll U$.[32] We

propose that tunneling of the magnetization is hindered and likely minimized in 2 due to the almost ideal C_3 symmetry of the cluster;[31] in addition the lack of nuclear spin at iron may hinder tunneling as proposed elsewhere.[43]

The structural reorganization upon one-electron reduction of (^{tbs}L)Fe$_3$(thf), the large comproportionation constant, and lack of an observable IVCT all strongly suggest a strongly delocalized mixed-valent electronic structure for the anionic cluster [(^{tbs}L)Fe$_3$]$^-$. The high and low temperature (acquired in a 2-MeTHF glass) ^{57}Fe Mössbauer spectra obtained corroborate this assignment. Moreover, the magnetometry data can be described at all temperatures (1.8–300 K) by a single spin electronic configuration where the intracore M–M bonding can be rationalized by a delocalized molecular orbital approach.

To construct a qualitative molecular orbital (MO) diagram for the cluster [(^{tbs}L)Fe$_3$]$^-$, we consider mixing the 15 valence Fe 3d and 9 valence N 2p orbitals using symmetry considerations, assuming the highest possible symmetry for the [(^{tbs}L)Fe$_3$]$^-$ anion. Each iron site in **1** (and **2**) resides nominally in a T-shape geometry; defining the local geometric *x* and *y* axes and, thus, the orientation of the respective $d_{x^2-y^2}$ orbital, along the Fe–N bonding vectors (e.g., Fe–N$_{anilido}$ = *x* axis, Fe–N$_{basal\ amido}$ = *y* axis, Figure 4). Thus, each local *z*-axis (and respective d$_{z^2}$ orbital) is normal to the individual *xy* planes, on average 52° with respect to the triiron plane. Under C_3 symmetry, the symmetry adapted linear combinations (SALCs) of the available 15 d orbitals transform as 5A + 5E. Combining these valence metal SALCs with the corresponding N-based SALCs of appropriate symmetry gives rise to the relative energetic ordering presented in Figure 4 (*Note:* the Fe–N bonding orbital configurations are omitted from the frontier analysis). The molecular orbital configurations are ranked energetically based on the apparent degree of orbital overlap and the type of bonding or antibonding interaction they afford. Population of the 15 orbital combinations with the 19 valence electrons results in the observed $S = {}^{11}/_{2}$ electronic configuration that has been experimentally determined for complex **2**.

5. CONCLUSIONS

The effect of electron delocalization has been documented in biological[6a,d,44] and synthetic[8,9,37e,45] polynuclear clusters where double exchange has been invoked as the mechanism through which high spin states are achieved. Herein we report the synthetic cluster [M][(^{tbs}L)Fe$_3$] ([M]$^+$ = [(18-C-6)K(thf)$_2$]$^+$ (**1**) or [(crypt-222)K]$^+$ (**2**)), a fully delocalized mixed-valent cluster that adopts a high spin electronic configuration. We propose the cluster geometric reorganization directs the metal valence orbitals to maximize intracore M–M bonding. Thus, the direct exchange interaction responsible for (^{tbs}L)Fe$_3$(thf) adopting a high spin configuration is enhanced (intracore Fe–Fe contraction) in the anion [(^{tbs}L)Fe$_3$]$^-$, consistent with the observed thermally persistent high spin ground state. This is analogous to the localized-to-delocalized transition found in mixed-valent Ferredoxin-type clusters [2Fe2S]^n where an $S = {}^{9}/_{2}$ state has been proposed to arise at low temperature (<80 K) from conformational changes in the wild-type protein.[46] Furthermore, the optimized metal valence orbital overlap provides the orbital pathway through which intervalence electron delocalization (i.e., double exchange) occurs. Maximizing the electron exchange

within the mixed-valent cluster compensates for the loss of the exogenous $2e^-$-donor solvent, affording the cluster its electronic stability (large K_c), and emergent single molecule magnet behavior. While the anisotropy recorded does not approach record barriers reported to date,[47] this and recent work[24] suggest a new molecular architecture where M–M bonding provides the conduit through which desirable magnetic properties can be attained. Research is under way to probe if this geometric reorganization and maximizing of the overall exchange interaction is unique to iron or can be observed with other metal combinations. Finally, future work will target understanding the origins of magnetic anisotropy exhibited by strongly delocalized mixed-valent clusters typified by $[(^{tbs}L)Fe_3]^-$ and other high-spin systems.[24]

Supplementary Material

Refer to Web version on PubMed Central for supplementary material.

Acknowledgments

This work was supported by a grant from the NIH (GM 098395), DOE (DE-SC0008313), and Harvard University.

R.H.S. gratefully acknowledges Consejo Nacional de Ciencia y Tecnología (CONACYT) and Fundación México for a doctoral fellowship. A.K.B. is grateful for a Smith Family Graduate Science and Engineering Fellowship. T.M.P. is grateful for support from the Novartis Graduate Fellowship in Chemical Sciences for Minorities and Women and the Marie Hong fellowship. G.M. is grateful for an NSERC postdoctoral fellowship.

References

1. Powers TM, Fout AR, Zheng SL, Betley TA. J Am Chem Soc. 2011; 133:3336. [PubMed: 21332160]
2. (a) Ferreira KN, Iverson TM, Maghlaoui K, Barber J, Iwata S. Science. 2004; 303:1831. [PubMed: 14764885] (b) Seefeldt LC, Hoffman BM, Dean DR. Annu Rev Biochem. 2009; 78:701. [PubMed: 19489731]
3. Beinert H, Holm RH, Munck E. Science. 1997; 277:653. [PubMed: 9235882]
4. (a) Siegbahn PEM. Acc Chem Res. 2009; 42:1871. [PubMed: 19856959] (b) Burgess BK, Lowe DJ. Chem Rev. 1996; 96:2983. [PubMed: 11848849]
5. (a) Zener C. Phys Rev. 1951; 82:403.(b) Anderson PW, Hasegawa H. Phys Rev. 1955; 100:675.
6. (a) Papaefthymiou V, Girerd JJ, Moura I, Moura JJG, Munck E. J Am Chem Soc. 1987; 109:4703. (b) Blondin G, Girerd JJ. Chem Rev. 1990; 90:1359.(c) Noodleman L, Peng CY, Case DA, Mouesca JM. Coord Chem Rev. 1995; 144:199.(d) Achim C, Golinelli MP, Bominaar EL, Meyer J, Munck E. J Am Chem Soc. 1996; 118:8168.
7. Girerd JJ. J Chem Phys. 1983; 79:1766.
8. Bechlars B, D'Alessandro DM, Jenkins DM, Iavarone AT, Glover SD, Kubiak CP, Long JR. Nat Chem. 2010; 2:362. [PubMed: 20414235]
9. (a) Drueke S, Chaudhuri P, Pohl K, Wieghardt K, Ding XQ, Bill E, Sawaryn A, Trautwein AX, Winkler H, Gurman SJ. J Chem Soc, Chem Commun. 1989; 59(b) Ding XQ, Bominaar EL, Bill E, Winkler H, Trautwein AX, Drueke S, Chaudhuri P, Wieghardt K. J Chem Phys. 1990; 92:178.(c) Gamelin DR, Bominaar EL, Kirk ML, Wieghardt K, Solomon EI. J Am Chem Soc. 1996; 118:8085. (d) Cotton FA, Daniels LM, Falvello LR, Murillo CA. Inorg Chim Acta. 1994; 219:7.(e) Cotton FA, Daniels LM, Maloney DJ, Murillo CA. Inorg Chim Acta. 1996; 249:9.(f) Cotton FA, Daniels LM, Falvello LR, Matonic JH, Murillo CA. Inorg Chim Acta. 1997; 256:269.(g) Zall CM, Zherebetskyy D, Dzubak AL, Bill E, Gagliardi L, Lu CC. Inorg Chem. 2012; 51:728. [PubMed: 22148181] (h) Zall CM, Clouston LJ, Young VG, Ding KY, Kim HJ, Zherebetskyy D, Chen YS, Bill E, Gagliardi L, Lu CC. Inorg Chem. 2013; 52:9216. [PubMed: 23902538]
10. Lee D, Krebs C, Huynh BH, Hendrich MP, Lippard SJ. J Am Chem Soc. 2000; 122:5000.

11. Cotton, FA., Murillo, CA., Walton, RA. Multiple Bonds Between Metal Atoms. Springer; 2005.
12. Zhao QL, Betley TA. Angew Chem Int Ed. 2011; 50:709.
13. Zhao QL, Harris TD, Betley TA. J Am Chem Soc. 2011; 133:8293. [PubMed: 21561083]
14. Eames EV, Harris TD, Betley TA. Chem Sci. 2012; 3:407.
15. (a) Harris TD, Zhao QL, Hernández Sánchez R, Betley TA. Chem Commun. 2011; 47:6344.(b) Fout AR, Xiao DJ, Zhao QL, Harris TD, King ER, Eames EV, Zheng SL, Betley TA. Inorg Chem. 2012; 51:10290. [PubMed: 22991939] (c) Eames EV, Betley TA. Inorg Chem. 2012; 51:10274. [PubMed: 22988949] (d) Eames EV, Hernández Sánchez R, Betley TA. Inorg Chem. 2013; 52:5006. [PubMed: 23642178]
16. (a) Fout AR, Zhao QL, Xiao DNJ, Betley TA. J Am Chem Soc. 2011; 133:16750. [PubMed: 21942370] (b) Powers TM, Betley TA. J Am Chem Soc. 2013; 135:12289. [PubMed: 23865953]
17. Lalancet JM, Rollin G, Dumas P. Can J Chem. 1972; 50:3058.
18. APEX2, v.2009. Bruker Analytical X-Ray Systems, Inc; Madison, WI: 2009.
19. Sheldrick, GM. SADABS, Version 2.03. Bruker Analytical X-Ray Systems, Inc; Madison, WI: 2000.
20. Spek, AL. PLATON, A Multipurpose Crystallographic Tool. Utrecht University; Utrecht, The Netherlands: 2010.
21. Sheldrick, GM. SHELXTL, Version 6.12. Bruker Analytical X-Ray Systems, Inc; Madison, WI: 2000.
22. Prisecaru, I. WMOSS4 Mössbauer Spectral Analysis Software. 2013. http://www.wmoss.org
23. Chilton NF, Anderson RP, Turner LD, Soncini A, Murray KS. J Comput Chem. 2013; 34:1164. [PubMed: 23386394]
24. Hernández Sánchez R, Betley TA. J Am Chem Soc. 2015; 137:13949. [PubMed: 26440452]
25. Ward MD. Chem Soc Rev. 1995; 24:121.
26. (a) LeSuer RJ, Geiger WE. Angew Chem Int Ed. 2000; 39:248.(b) Ohrenberg C, Geiger WE. Inorg Chem. 2000; 39:2948. [PubMed: 11232836] (c) Yeomans BD, Kelso LS, Tregloan PA, Keene FR. Eur J Inorg Chem. 2001; 2001:239.(d) Barriere F, Camire N, Geiger WE, Mueller-Westerhoff UT, Sanders R. J Am Chem Soc. 2002; 124:7262. [PubMed: 12071722] (e) D'alessandro DM, Keene FR. Dalton Trans. 2004; 3950
27. Allen, GC., Hush, NS. Prog Inorg Chem. John Wiley & Sons, Inc; 1967. p. 357
28. (a) Hush, NS. Prog Inorg Chem. John Wiley & Sons, Inc; 1967. p. 391(b) Hush NS. Electrochim Acta. 1968; 13:1005.
29. Robin, MB., Day, P. Adv Inorg Chem Radiochem. Emeléus, HJ., Sharpe, AG., editors. Vol. 10. Academic Press; 1968. p. 247
30. Demadis KD, Hartshorn CM, Meyer TJ. Chem Rev. 2001; 101:2655. [PubMed: 11749392]
31. Glaser T, Heidemeier M, Weyhermuller T, Hoffmann RD, Rupp H, Muller P. Angew Chem Int Ed. 2006; 45:6033.
32. Gatteschi, D., Sessoli, R., Villain, J. Molecular Nanomagnets. OUP; Oxford: 2006.
33. Guo YN, Xu GF, Guo Y, Tang JK. Dalton Trans. 2011; 40:9953. [PubMed: 21829790]
34. Cole KS, Cole RH. J Chem Phys. 1941; 9:341.
35. Aubin SMJ, Sun ZM, Pardi L, Krzystek J, Folting K, Brunel LC, Rheingold AL, Christou G, Hendrickson DN. Inorg Chem. 1999; 38:5329.
36. Yang, P. The Chemistry of Nanostructured Materials. World Scientific; 2003.
37. (a) Dutta SK, Ensling J, Werner R, Florke U, Haase W, Gutlich P, Nag K. Angew Chem Int Ed Engl. 1997; 36:152.(b) Reiff WM, LaPointe AM, Witten EH. J Am Chem Soc. 2004; 126:10206. [PubMed: 15315408] (c) Merrill WA, Stich TA, Brynda M, Yeagle GJ, Fettinger JC, De Hont R, Reiff WM, Schulz CE, Britt RD, Power PP. J Am Chem Soc. 2009; 131:12693. [PubMed: 19670870] (d) Harman WH, Harris TD, Freedman DE, Fong H, Chang A, Rinehart JD, Ozarowski A, Sougrati MT, Grandjean F, Long GJ, Long JR, Chang CJ. J Am Chem Soc. 2010; 132:18115. [PubMed: 21141856] (e) Hazra S, Sasmal S, Fleck M, Grandjean F, Sougrati MT, Ghosh M, Harris TD, Bonville P, Long GJ, Mohanta S. J Chem Phys. 2011; 134:174507. [PubMed: 21548699] (f) Zadrozny JM, Xiao DJ, Long JR, Atanasov M, Neese F, Grandjean F, Long GJ. Inorg Chem. 2013; 52:13123. [PubMed: 24175913] (g) Zadrozny JM, Xiao DJ, Atanasov M, Long GJ, Grandjean F,

Neese F, Long JR. Nat Chem. 2013; 5:577. [PubMed: 23787747] (h) Jeon IR, Park JG, Xiao DJ, Harris TD. J Am Chem Soc. 2013; 135:16845. [PubMed: 24164631] (i) Bryan AM, Lin CY, Sorai M, Miyazaki Y, Hoyt HM, Hablutzel A, LaPointe A, Reiff WM, Power PP, Schulz CE. Inorg Chem. 2014; 53:12100. [PubMed: 25368962]

38. Schulz CE, Hu CJ, Scheidt WR. Hyperfine Interact. 2006; 170:55. [PubMed: 18160971]
39. D'alessandro DM, Keene FR. Chem Soc Rev. 2006; 35:424. [PubMed: 16636726]
40. Moushi EE, Stamatatos TC, Wernsdorfer W, Nastopoulos V, Christou G, Tasiopoulos AJ. Inorg Chem. 2009; 48:5049. [PubMed: 19072669]
41. Sessoli R, Tsai HL, Schake AR, Wang SY, Vincent JB, Folting K, Gatteschi D, Christou G, Hendrickson DN. J Am Chem Soc. 1993; 115:1804.
42. (a) Christou G, Gatteschi D, Hendrickson DN, Sessoli R. MRS Bull. 2000; 25:66.(b) Soler M, Wernsdorfer W, Folting K, Pink M, Christou G. J Am Chem Soc. 2004; 126:2156. [PubMed: 14971951]
43. Fataftah MS, Zadrozny JM, Rogers DM, Freedman DE. Inorg Chem. 2014; 53:10716. [PubMed: 25198379]
44. (a) Pierik AJ, Hagen WR. Eur J Biochem. 1991; 195:505. [PubMed: 1847685] (b) Hagen WR. Adv Inorg Chem. 1992; 38:165.(c) Pierik AJ, Hagen WR, Dunham WR, Sands RH. Eur J Biochem. 1992; 206:705. [PubMed: 1318833]
45. Bencini A, Palii AV, Ostrovsky SM, Tsukerblat BS, Uytterhoeven MG. Mol Phys. 1995; 86:1085.
46. Achim C, Bominaar EL, Meyer J, Peterson J, Munck E. J Am Chem Soc. 1999; 121:3704.
47. (a) Layfield RA. Organometallics. 2014; 33:1084.(b) Craig GA, Murrie M. Chem Soc Rev. 2015; 44:2135. [PubMed: 25716220]

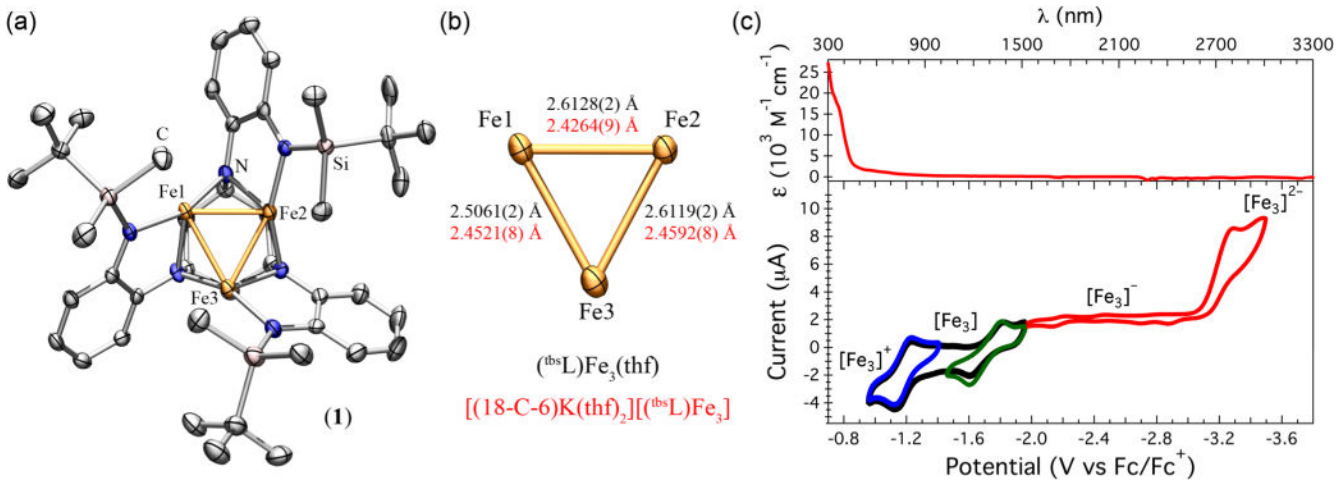

Figure 1.

(a) Molecular crystal structure of $[(18\text{-C-6})K(thf)_2][(^{tbs}L)Fe_3]$ (**1**) viewed along the anion's C_3 axis. The hydrogen atoms and the countercation $[(18\text{-C-6})K(thf)_2]^+$ have been omitted for clarity. Thermal ellipsoids are set at 50% probability level. (b) Comparison of the structural metrics of the trinuclear core $[Fe_3]$ of the neutral all-ferrous $(^{tbs}L)Fe_3(thf)$[1] and one-electron reduced cluster in **1**. The Fe1 site corresponds to the THF-solvated site in $(^{tbs}L)Fe_3(thf)$. (c) Top: UV−vis−NIR spectrum of **1** in THF. Bottom: cyclic voltammogram displaying three electrochemical events at $E_{1/2}$ (ΔE_p) = −1.18 (109 mV), −1.71 (219 mV), and E_{pc} = −3.29 V vs Fc/Fc^+. The red trace is offset by +2 μA. Scan rate for all scans: 20 mV/s.

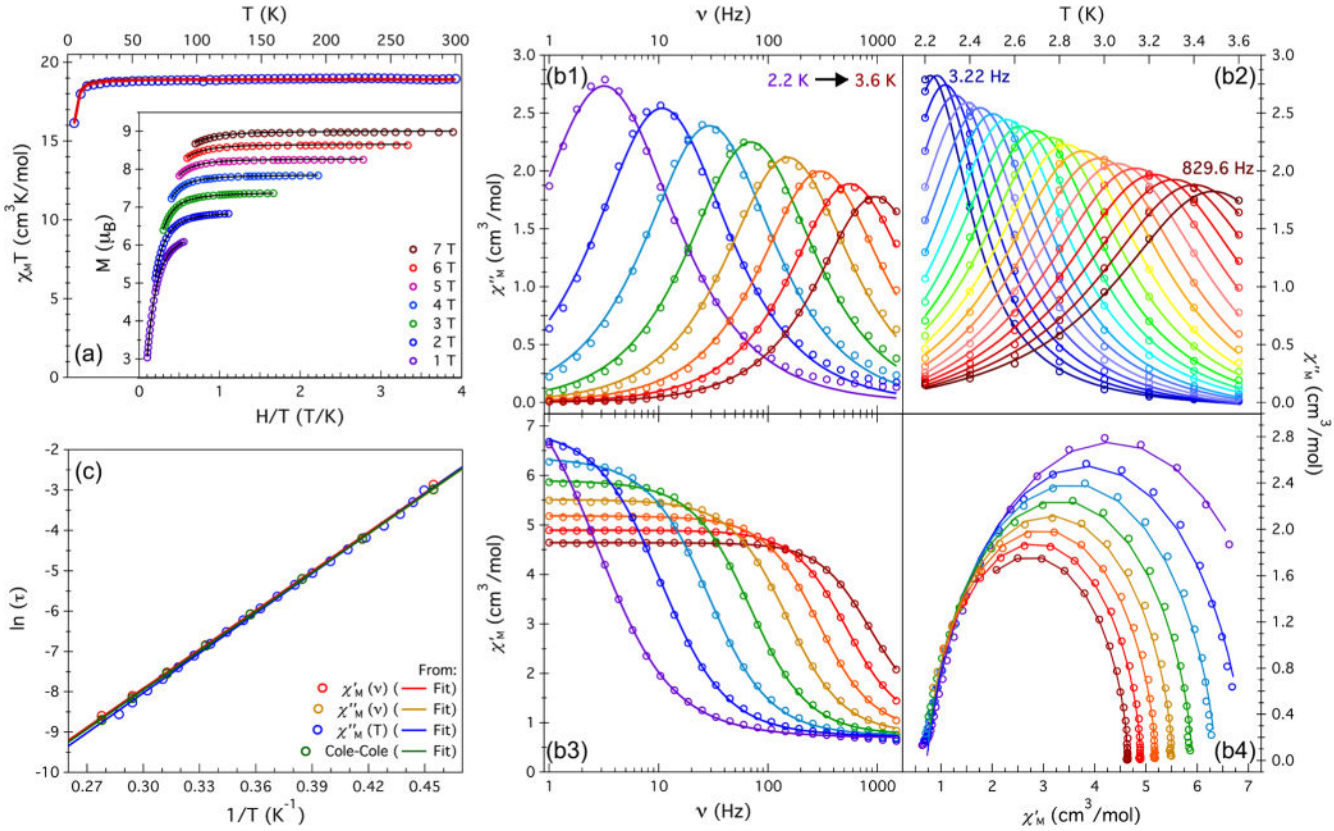

Figure 2.

Magnetic characterization of [(crypt-222)K][(^{tbs}L)Fe$_3$] (**2**). (a) VT dc magnetic susceptibility collected at 0.5 T (blue circles). Inset: VTVH magnetization data collected on increasing temperature from 1.8 to 10 K at increasing field from 1 to 7 T. (b1–b4) Slow magnetic relaxation phenomena: out-of-phase (χ''_M, b1 and in-phase (χ'_M, b3 components of the magnetic susceptibility vs frequency (ν); (b2) χ''_M vs T; and (b4) Cole–Cole plots. (c) Relaxation times (ln τ) extracted from the independent fit of the data in panels (b1–b4) vs $1/T$. The continuous red and black in (a), and color-coded traces in (b1–b4 and c) represent a fit to the data as described in the text.

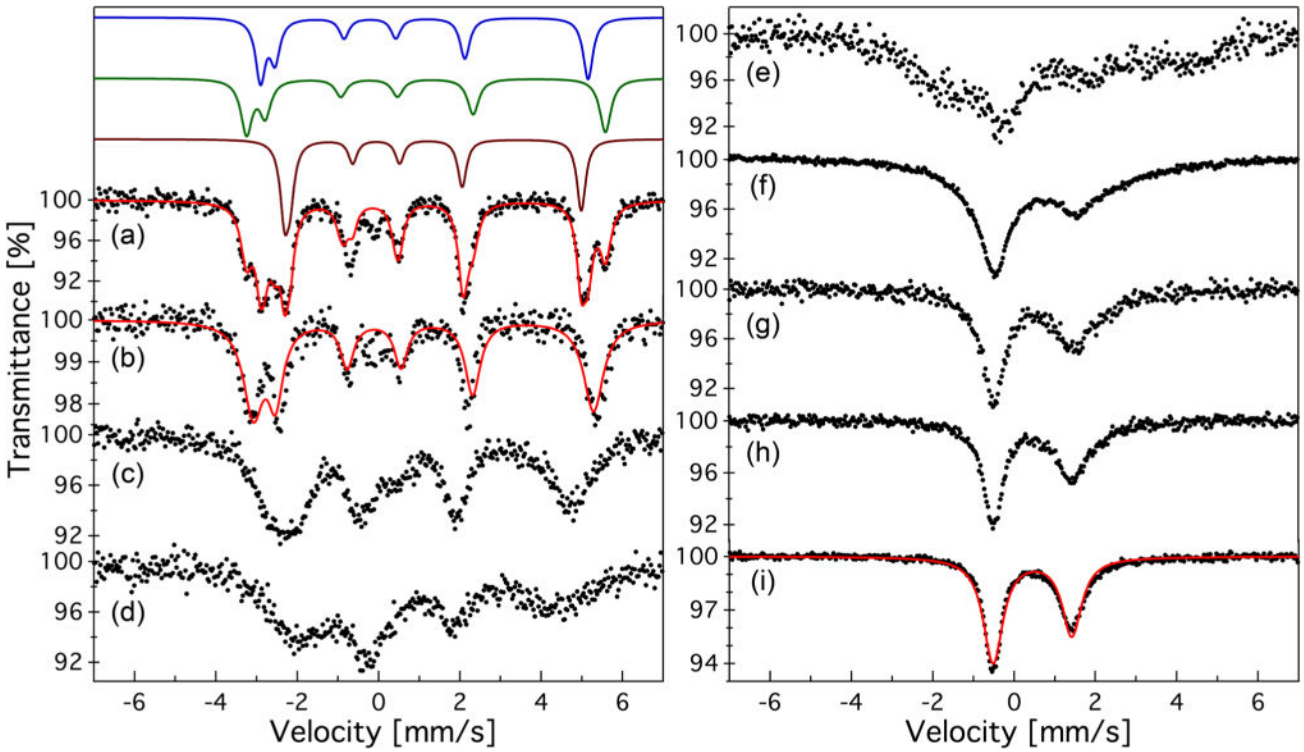

Figure 3.

Variable-temperature zero-field ^{57}Fe Mössbauer spectra of [(18-C-6)K(thf)$_2$][(^{tbs}L)Fe$_3$] (**1**). Data was collected at the following temperatures: (a, b) 4.2, (c) 20, (d) 30, (e) 40, (f) 90, (g) 130, (h) 170, and (i) 210 K. Data in (a) was obtained from a polycrystalline sample while that in (b) was acquired from a sample in a frozen glass using 2-methyltetrahydrofuran. The red traces in (a), (b), and (i) correspond to the overall fit, while the brown, green and blue traces above (a) are the three sextets employed to fit (a). The fit parameters are described according to the model described in the text.

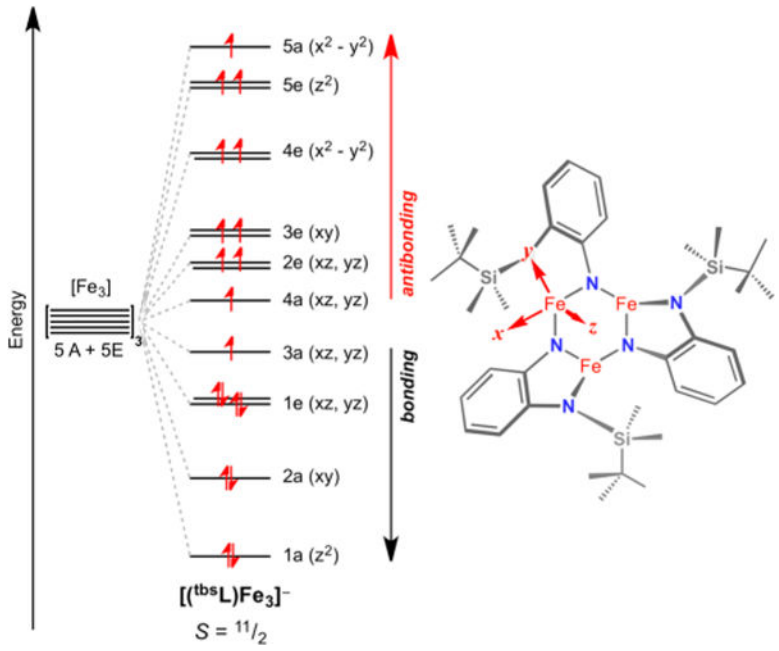

Figure 4.

Qualitative molecular orbital for the anion $[(^{tbs}L)Fe_3]^-$ (in **1** and **2**) assuming ideal C_3 symmetry. Note the bonding and antibonding designations describe the M–M orbital overlap interactions.

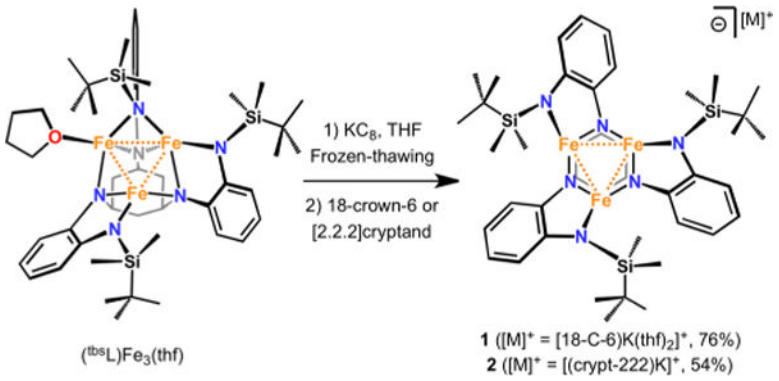

Scheme 1.